











**Robust spin injection via thermal magnon pumping in antiferromagnet/ferromagnet hybrid systems**Rodolfo Rodriguez <sup>1</sup>, Shirash Regmi <sup>1</sup>, Hantao Zhang <sup>2</sup>, Wei Yuan <sup>1</sup>, Pavlo Makushko,<sup>3</sup> Eric A. Montoya <sup>4,5</sup>, Ihor Veremchuk,<sup>3</sup> René Hübner <sup>3</sup>, Denys Makarov <sup>3</sup>, Jing Shi <sup>1</sup>, Ran Cheng <sup>2,1</sup> and Igor Barsukov <sup>1,\*</sup><sup>1</sup>Department of Physics and Astronomy, University of California, Riverside, California 92521, USA<sup>2</sup>Department of Electrical and Computer Engineering, University of California, Riverside, California 92521, USA<sup>3</sup>Helmholtz-Zentrum Dresden-Rossendorf e.V., Institute of Ion Beam Physics and Materials Research, 01328 Dresden, Germany<sup>4</sup>Department of Physics and Astronomy, University of Utah, Salt Lake City, Utah 84112, USA<sup>5</sup>Department of Physics and Astronomy, University of California, Irvine, California 92697, USA

(Received 7 January 2022; revised 10 May 2022; accepted 13 July 2022; published 22 August 2022)

Robust spin injection and detection in antiferromagnetic thin films is a prerequisite for the exploration of antiferromagnetic spin dynamics and the development of nanoscale antiferromagnet-based spintronic applications. Previous studies have shown spin injection and detection in antiferromagnet/nonmagnetic metal bilayers; however, spin injection in these systems has been found effective at cryogenic temperatures only. Here, we experimentally demonstrate sizable interfacial spin transport in a hybrid antiferromagnet/ferromagnet system, consisting of  $\text{Cr}_2\text{O}_3$  and permalloy, which remains robust up to the room temperature. We examine our experimental data within a spin diffusion model and find evidence for the important role of interfacial magnon pumping in the signal generation. The results bridge spin-orbitronic phenomena of ferromagnetic metals with antiferromagnetic spintronics and demonstrate an advancement toward antiferromagnetic spin-torque devices.

DOI: [10.1103/PhysRevResearch.4.033139](https://doi.org/10.1103/PhysRevResearch.4.033139)**I. INTRODUCTION**

With their robustness against perturbation to magnetic fields and ultrafast spin dynamics, antiferromagnets (AFMs) are at the forefront of spintronics research as promising material candidates. However, efficient manipulation and readout of antiferromagnetic spin dynamics remains a major challenge [1]. Antiferromagnetic insulators [2], being of particular interest due to absent electrical shunting and low magnetic dissipation, rely on interfacial spin-charge conversion [3–7]. AFM/NM interfaces, where NM is a nonmagnetic metal with large spin-orbit coupling (e.g., Pt), have been used for accessing magnetic order [8,9] via spin Hall magnetoresistance. Furthermore, Néel vector switching has been observed in multiterminal AFM/NM devices [10–15], whereby thermal, structural, and spin-orbit phenomena have been discussed [16]. In studies of spin transport through ultra-thin AFM layers between NM and a ferromagnet, contributions of spin fluctuations and coherent evanescent spin waves have been investigated [17–20]. In spin Seebeck experiments [21–24], thermally driven spin currents across the spin-flop (SF) transition in the easy-axis AFM  $\text{Cr}_2\text{O}_3$  have been observed [25,26]. These works have shown that the interfacial spin mixing conductance decreases substantially with increasing temperature [27] – an observation that is in agreement with temperature-dependent spin pumping mea-

surements in AFM/NM at sub-THz and GHz frequencies [25,28] and underlines the challenges of functionalizing AFM/NM interfaces for spintronic applications [1].

Ferromagnetic (FM) metals have recently gained attention due to the versatility of spin-orbitronic phenomena inherent to them [29,30]. Theoretical [29,31,32] and experimental works [33,34] on planar Hall and anomalous Hall spin injection have sparked interest for ferromagnetic metals as tunable spin injectors and detectors. Observation of magnetization-tunable spin torques in two-magnet bilayers and FM/NM multilayers [35] and recent formulation of the spin-dependent anomalous Hall effect [32,36] underline the potential of ferromagnetic metals as efficient spin-charge converters. Realization of magnetic autooscillations driven by thermal spin currents [37] as well as magnon-magnon coupling and transduction [18,38–43] further substantiate the technological relevance of the two-magnet architecture concept and raise the question whether antiferromagnet-ferromagnet hybrids have potential for the development of functional AFM-based spin-torque devices.

Here, we experimentally demonstrate thermal spin injection from a ferromagnetic metal, permalloy ( $\text{Py} = \text{Ni}_{80}\text{Fe}_{20}$ ), into a thin film of an insulating antiferromagnet,  $\text{Cr}_2\text{O}_3$ . We observe magnonic pumping with different spin across the SF transition that allows for sizable signals at room temperature. The results show promise for spintronics applications that take advantage of both antiferromagnetic spin dynamics and spin-orbitronic concepts inherent to ferromagnetic metals and pave the way toward AFM-FM hybrid spin-torque devices.

**II. EXPERIMENT**

We grow 100 nm thin  $\text{Cr}_2\text{O}_3$  films [24] on  $m$ -plane ( $10\bar{1}0$ ) sapphire ( $\text{Al}_2\text{O}_3$ ) substrates [Fig. 1(a)] using rf-magnetron

\*igor@ucr.edu

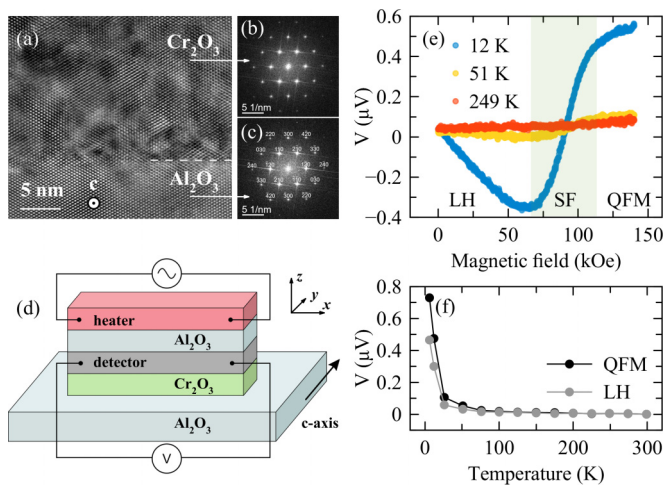


FIG. 1. (a) Cross-sectional transmission electron micrograph of the  $m$ -plane  $\text{Al}_2\text{O}_3/\text{Cr}_2\text{O}_3$  interface with the  $c$ -axis [0001]-oriented out of the page and (b,c) the corresponding diffractograms of  $\text{Cr}_2\text{O}_3$  and  $\text{Al}_2\text{O}_3$  indicating epitaxial order. (d) Sample geometry. The magnetic field is applied parallel to the  $c$ -axis. (e) Spin Seebeck (SSE) voltage of the  $\text{Cr}_2\text{O}_3/\text{Pt}$  sample shows a sign change across the SF transition. (f) SSE signals dominated by left-hand (LH) and quasiferromagnetic (QFM) magnons fall rapidly with increasing temperature.

sputter deposition. The films reveal epitaxial growth, a well-defined  $c$ -axis [0001] within the film plane [Figs. 1(b) and 1(c)], and have a typical surface roughness of 0.5 nm. The films are capped with one of three types of spin current detector layer using magnetron sputtering: (i) a nonmagnetic detector layer (4 nm)Pt, (ii) a ferromagnetic detector layer (5 nm)Py, and (iii) a combination detector layer (5 nm)Py/(2 nm)Pt. The multilayers are structured into  $2.4 \times 0.25 \text{ mm}^2$  bars using optical lithography and ion milling. The axis of the bar is perpendicular to the  $c$ -axis of  $\text{Cr}_2\text{O}_3$ . An electrically insulating (80 nm)  $\text{Al}_2\text{O}_3$  buffer layer is deposited using atomic layer deposition. Finally, a metallic heater is deposited onto the buffer layer, with the same dimensions and lateral position as the underlying detector bar [Fig. 1(d)]. The goal of the above procedure is to obtain three sets of directly comparable devices that differ by choice of the spin current detector layer. A low-frequency electric current of 3 mA (rms) is supplied to the heater, resulting in a dissipated power of  $\sim 4 \text{ mW}$  and in a periodic temperature gradient across the  $\text{Cr}_2\text{O}_3/\text{detector}$  interface. The voltage generated by the detector layer is measured on the current's second harmonic using a lock-in amplifier. The measurements are performed in a cryostat with bath temperature  $T$  and carried out with the same experiment parameters for all samples.

In the  $\text{Cr}_2\text{O}_3/\text{Pt}$  bilayer, the temperature gradient leads to an interfacial spin current which is converted into a voltage signal  $V$  via inverse spin Hall effect (iSHE) [44,45]. The SHE symmetry requires the spin polarization and thus the  $c$ -axis of  $\text{Cr}_2\text{O}_3$  to lie within the film plane, as realized in our  $m$ -plane films. This spin Seebeck signal is shown in Fig. 1(e) as a function of magnetic field  $H$  applied parallel to the  $c$ -axis. The plot shows three distinct field regimes. At low fields, the spin current is dominated by the lowest-energy antiferromagnetic magnons [27,46] of  $\text{Cr}_2\text{O}_3$  [Fig. 4(c)]. These are left-handed

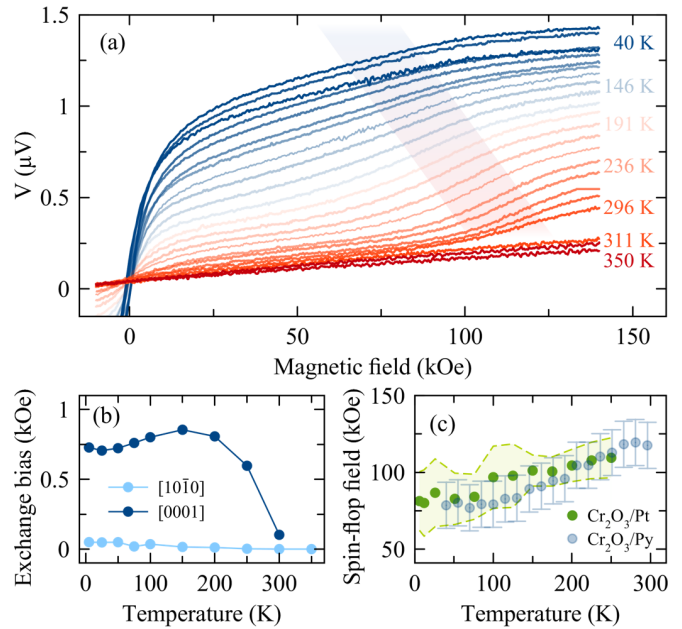


FIG. 2. (a) Thermally induced signal of the  $\text{Cr}_2\text{O}_3/\text{Py}$  sample as a function of magnetic field. The  $\text{Cr}_2\text{O}_3$ -related signal is superimposed on the sigmoidlike anomalous Nernst signal of Py magnetization reversal and disappears at the Néel temperature. The SF field region is indicated by the shading. (b) Exchange-bias field of a  $\text{Cr}_2\text{O}_3/\text{Py}$  sample measured perpendicular and parallel to the  $c$ -axis. (c) The SF field regions of the  $\text{Cr}_2\text{O}_3/\text{Pt}$  and  $\text{Cr}_2\text{O}_3/\text{Py}$  samples overlap.

(LH) magnons with  $-\hbar$  spin and generate a negative signal. With increasing magnetic field, the uniaxial two-sublattice spin system of  $\text{Cr}_2\text{O}_3$  undergoes a SF transition, leading to a sign reversal of the spin Seebeck signal. Above the SF field, the spin current is dominated by the quasiferromagnetic (QFM) magnons which carry spin  $+\hbar$ . Starting from  $T = 11 \text{ K}$ , with increasing bath temperature, both the LH and QFM signals rapidly fall, as shown in Fig. 1(f). At room temperature the signal is negligibly small (which is consistent with previous findings [26]). The spin transport at the AFM/NM interface is robust only in the narrow range of low temperatures.

For the  $\text{Cr}_2\text{O}_3/\text{Py}$  bilayer, as shown in Fig. 2(a), the thermally generated signal is dominated by the sigmoidlike shape due the anomalous Nernst effect (ANE) of Py [47,48]. With magnetic field traversing through zero, Py magnetization undergoes a reversal, which is translated by the temperature gradient across the Py layer into a sign change of the voltage signal. In a control sample of a Py bar deposited directly on an  $m$ -plane  $\text{Al}_2\text{O}_3$  substrate, as expected, a steplike ANE signal is observed (see the Appendix). In the  $\text{Cr}_2\text{O}_3/\text{Py}$  bilayer, on the other hand, the signal approaches saturation over the entire field range. Such high-field saturation effects have been studied in ferromagnetic thin films [49–51] and discussed to originate from interfacial spin pinning. We carry out exchange-bias measurements in  $\text{Cr}_2\text{O}_3/\text{Py}$  bilayer films. The observed exchange-bias field of  $\lesssim 800 \text{ Oe}$  along the  $c$ -axis, shown in Fig. 2(b), corroborates the hypothesis of the interfacial pinning of Py spins [52,53].

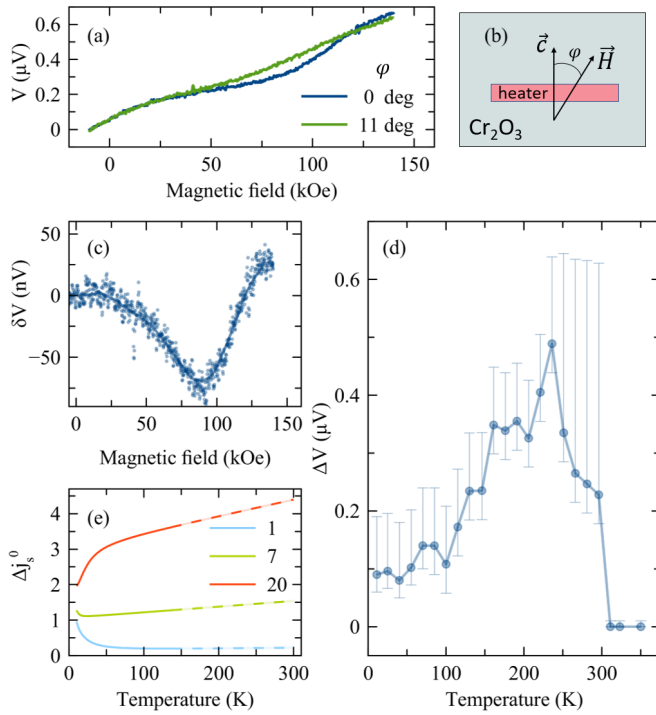


FIG. 3. (a) Thermally generated signal of  $\text{Cr}_2\text{O}_3/\text{Py}$  as a function of magnetic field applied at angle  $\phi$  with respect to the  $c$ -axis of  $\text{Cr}_2\text{O}_3$ , as shown in the top view of the device (b). (c) Difference between the thermally generated spectra with aligned and misaligned magnetic field approximates the SSE signal, which shows a sign change across the SF transition. (d) SSE voltage jump across the SF transition in  $\text{Cr}_2\text{O}_3/\text{Py}$  increases with increasing temperature, before collapsing at the Néel temperature. (e) Injected spin current jump across the SF transition (in arbitrary units) is calculated for various ratios  $g_m^\uparrow/g_n^\uparrow$  of the spin transmission coefficients. Dashed lines represent an extension of the theory based on the magnon approximation to high temperatures.

Superimposed on the ANE signal of Py, another conspicuous signal introduces an inflection point in the 80–120 kOe field range [shaded region in Fig. 2(c)]. The inflection point field increases with increasing temperature; it follows the SF field [54], shown in Fig. 2(c), which we extract from measurements on  $\text{Cr}_2\text{O}_3/\text{Pt}$  where the signal is not obscured by the ANE contributions. Moreover, the superimposed signal disappears in the temperature range of 296–311 K [Fig. 2(a)], where we find the Néel temperature  $T_N = 305$  K of the  $\text{Cr}_2\text{O}_3$  film [55]. Remarkably, the signal first increases with increasing temperature before collapsing at the Néel temperature, even though the underlying ANE signal continuously decreases with increasing temperature. These observations confirm that the signal superimposed on the ANE sigmoid originates from the  $\text{Cr}_2\text{O}_3$  spin system and its mechanism is different from ANE. We refer to it as the spin Seebeck (SSE) signal.

The ANE background in conjunction with the interfacial pinning does not allow for an exact quantitative determination of the  $\text{Cr}_2\text{O}_3$ -related SSE signal. We therefore employ two holistic methods for its assessment: (i) At 240 K, we intentionally misalign the magnetic field direction with respect to the  $c$ -axis of  $\text{Cr}_2\text{O}_3$  by up to  $\phi = 11^\circ$ , as shown in Figs. 3(a) and

3(b). Such misalignment leads to a partial suppression of the SSE signals [56]. We then subtract the misaligned spectrum from the aligned one. This procedure cannot be used to fully subtract the underlying ANE signal, due to a residual SSE signal in the misaligned geometry and the angle-dependent nature of the the ANE signal, and provides a qualitative assessment of the SSE signal. The resultant difference curve  $\delta V$  [Fig. 3(c)] first decreases and then increases with increasing magnetic field, similarly to the SSE signal of  $\text{Cr}_2\text{O}_3/\text{Pt}$  in Fig. 1(e). The  $\delta V$  difference spectrum confirms that the SSE signal in fact shows a sign change across the SF field, the latter being in agreement with the data shown in Fig. 2(c). (ii) We graphically extract the signal difference  $\Delta V$  by simply taking the values of  $V$  below and above the SF from the field-dependent data of Fig. 2(a). While this procedure imposes a notable systematic error to the data (see the Appendix), it affirms the temperature dependence of the SSE signal in  $\text{Cr}_2\text{O}_3/\text{Py}$  that was conspicuous from the raw data in Fig. 2(a): The signal increases with increasing temperature and collapses at the Néel temperature [Fig. 3(d)]. This behavior is in stark contrast to the thermal spin signal in  $\text{Cr}_2\text{O}_3/\text{Pt}$  which vanishes above 50 K. In the  $\text{Cr}_2\text{O}_3/\text{Py}$  hybrid system, the observed robust spin transport near room temperature is a prerequisite for practical AFM-based applications and calls upon a microscopic evaluation.

### III. THEORETICAL MODEL

We attribute the  $\text{Cr}_2\text{O}_3$ -related signal to the spin-dependent anomalous Hall effect (SAHE) [32] in Py, which converts the interfacial spin current into a transverse voltage, functioning as a spin detector. Under the device geometry depicted in Fig. 1(d), the spin-dependent electron transport in Py can be characterized by

$$j_x^\pm = -\sigma_\pm \frac{\partial \mu_\pm}{\partial x} + \theta_{\text{AH}}^\pm j_z^\pm + \Sigma_{\text{AN}}^\pm \frac{\partial T}{\partial z}, \quad (1)$$

$$j_z^\pm = -\sigma_\pm \frac{\partial \mu_\pm}{\partial z} - \theta_{\text{AH}}^\pm j_x^\pm, \quad (2)$$

where  $\pm$  represents spin-up/down polarization along the  $x$  direction and  $\mu_\pm$  is the spin-dependent chemical potential.  $\sigma_\pm$ ,  $\theta_{\text{AH}}^\pm$ ,  $\Sigma_{\text{AN}}^\pm$  are the spin-dependent electrical conductivity, anomalous Hall, and anomalous Nernst coefficients of the Py [21]. In the linear response regime, these quantities can be parametrized as  $\sigma_\pm = \sigma(1 \pm P)$ ,  $\theta_{\text{AH}}^\pm = \theta_{\text{AH}}(1 \pm \beta)$ , and  $\Sigma_{\text{AN}}^\pm = \Sigma_{\text{AN}}(1 \pm \alpha)$  [29], where  $P$ ,  $\beta$ , and  $\alpha$  are phenomenological constants.

Defining  $\mathbf{j}_c = \mathbf{j}^\uparrow + \mathbf{j}^\downarrow$  as the charge current density and  $\mathbf{j}_s = \mathbf{j}^\uparrow - \mathbf{j}^\downarrow$  as the spin current density, and using  $\mu_c = (\mu_\uparrow + \mu_\downarrow)/2$  as the charge chemical potential and  $\mu_s = (\mu_\uparrow - \mu_\downarrow)/2$  as the spin chemical potential, we can solve the continuity conditions  $\nabla \cdot \mathbf{j}_c + \partial \mu_c / \partial t = 0$  and  $\nabla \cdot \mathbf{j}_s + \partial \mu_s / \partial t = -\mu_s / \tau_s$ , where  $\tau_s$  is the spin relaxation time. Up to linear order in  $\partial T / \partial z$ ,  $P$ ,  $\beta$ , and  $\alpha$ , we obtain the spin diffusion equation and its solution as

$$\frac{\partial^2 \mu_s}{\partial z^2} = \frac{\mu_s}{\lambda^2}, \quad (3)$$

$$\mu_s = \frac{\lambda j_s^0 \cosh\left(\frac{z-d}{\lambda}\right)}{2\sigma \sinh\left(\frac{d}{\lambda}\right)}, \quad (4)$$

where  $\lambda \approx \sqrt{2\sigma\tau_s}$  is the spin diffusion length of the Py, and  $j_s^0$  is the interfacial spin current density injected from the  $\text{Cr}_2\text{O}_3$  into the Py which serves as the boundary condition for Eq. (3). We omit  $\partial^2\mu_s/\partial x^2$  term because the length of the Py bar is orders of magnitude larger than its thickness, suppressing the spin diffusion effect along  $y$  direction [29].

With the open circuit boundary condition of  $\mathbf{j}_c$  in the  $x$  direction and  $\partial\mu_c/\partial x \approx -\theta_{\text{AH}}(P + \beta)\partial\mu_s/\partial z - (\Sigma_{\text{AN}}/\sigma)\partial T/\partial z$ , the detected voltage along  $x$  averaged over the film thickness becomes

$$V = \frac{L\Sigma_{\text{AN}}}{\sigma d}\Delta T + \frac{L\lambda}{2\sigma d}\theta_{\text{AH}}(P + \beta)j_s^0 \tanh \frac{d}{2\lambda}, \quad (5)$$

where  $L$  and  $d$  are length and thickness of the Py bar, and  $\Delta T$  is the temperature drop across the thickness of Py. While the ANE background signal is independent of  $\text{Cr}_2\text{O}_3$  (except for interfacial spin pinning, as discussed above), the SAHE term depends on the interfacial spin injection  $j_s^0$  and hence on the Néel vector in  $\text{Cr}_2\text{O}_3$ .

The SF transition in  $\text{Cr}_2\text{O}_3$  directly leads to a sign change of  $j_s^0$ , because the reorientation of the Néel vector causes a reversal of the spin polarization of the lowest-energy magnon bands [25]. Following the formalism by Rietz *et al.* [27], we consider the spin pumping contributions by the Néel vector  $\mathbf{n}$  and finite magnetization moment  $\mathbf{m}$  as

$$\mathbf{j}_s^0 = g_n^{\uparrow\downarrow} \mathbf{n} \times \dot{\mathbf{n}} + g_m^{\uparrow\downarrow} \mathbf{m} \times \dot{\mathbf{m}}, \quad (6)$$

where  $g_n^{\uparrow\downarrow}$  and  $g_m^{\uparrow\downarrow}$  are the (real parts of) interfacial spin-mixing conductance for the Néel vector  $\mathbf{n}$  and total magnetic moment  $\mathbf{m}$ , respectively. By integrating the magnon modes over the Brillouin zone, we can obtain the total spin current  $j_s^0$  arising from the spin dynamics in  $\text{Cr}_2\text{O}_3$ . Across the SF transition,  $j_s^0$  experiences a sign change (see the Appendix), in agreement with experimental data in Fig. 3(c). Consequently, we calculate [Fig. 3(e)] the difference of spin injection across the SF transition,  $\Delta j_s^0$ , which allows for comparison with the  $\Delta V$  signal in Fig. 3(d).

#### IV. DISCUSSION

The distinct difference of the temperature dependence of thermally driven spin current in  $\text{Cr}_2\text{O}_3/\text{Py}$  [Fig. 3(d)] and  $\text{Cr}_2\text{O}_3/\text{Pt}$  [Fig. 1(f)] can be phenomenologically captured by the ratios of interfacial spin transmission coefficients  $g_m^{\uparrow\downarrow}/g_n^{\uparrow\downarrow}$  associated with the vectors  $\mathbf{m}$  and  $\mathbf{n}$  [57,58]. We do not expect the theoretical curves, calculated in Fig. 3(e), to accurately reproduce the experimental data of Figs. 1(f) and 3(d), but they allow us to assess the differences between the AFM/NM and AFM/FM systems qualitatively. As shown in Fig. 3(e),  $g_m^{\uparrow\downarrow}/g_n^{\uparrow\downarrow} = 20$  results in an increasing  $\Delta j_s^0$  with increasing temperature, while  $g_m^{\uparrow\downarrow}/g_n^{\uparrow\downarrow} = 1$  yields a decreasing  $\Delta j_s^0$ . The general trend of  $\Delta j_s^0$  under different  $g_m^{\uparrow\downarrow}/g_n^{\uparrow\downarrow}$  clearly indicates that this quantity is larger in  $\text{Cr}_2\text{O}_3/\text{Py}$  than in  $\text{Cr}_2\text{O}_3/\text{Pt}$ , especially at higher temperatures. A plausible mechanism underlying the enhanced value of  $g_m^{\uparrow\downarrow}/g_n^{\uparrow\downarrow}$  is that magnonic excitations in Py, which are absent in Pt, play an important role. The majority electrons have a spin polarization opposite to that of the magnonic excitations in Py. Below the SF transition in  $\text{Cr}_2\text{O}_3$ , the spin polarization of its lowest-energy magnon band matches that of the majority electrons but not

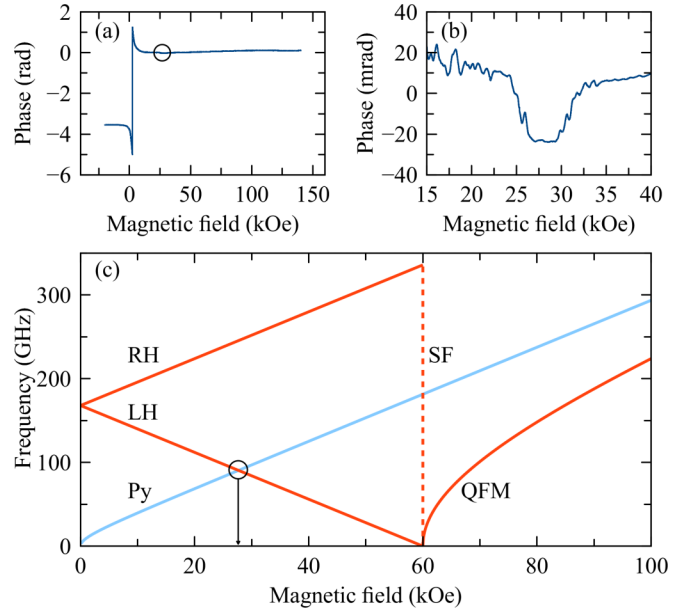


FIG. 4. (a), (b) Temporal phase of the thermal signal in  $\text{Cr}_2\text{O}_3/\text{Py}$  reveals an anomaly at  $\sim 30$  kOe. (c) Estimated frequencies of zero-wave-vector magnons in  $\text{Cr}_2\text{O}_3$  and Py as a function of magnetic field. Left-hand (LH), right-hand (RH), spin-flop (SF), and quasiferromagnetic (QFM) modes are shown. Py and LH magnons cross at  $\sim 30$  kOe.

the magnons in Py [25,28,59]. Therefore, the electrons in Py dominate the spin transmission processes while the magnon contribution is suppressed. Above the SF transition, on the other hand,  $\text{Cr}_2\text{O}_3$  develops a net magnetization along the applied magnetic field. The magnons in  $\text{Cr}_2\text{O}_3$  and in Py now have matching spin polarization, enabling the magnon-magnon spin transmission across the interface [40,41]. Once a magnon spin current in Py is generated, it drags the electron spin current, resulting in an effective enhancement of  $g_m^{\uparrow\downarrow}$ . This is in stark contrast to AFM/NM interfaces, where magnonic excitations in NM are absent [27].

This phenomenological explanation is further supported by an experimental observation that suggests a coupling between the magnonic subsystems of  $\text{Cr}_2\text{O}_3$  and Py. In Figs. 4(a) and 4(b) for  $\text{Cr}_2\text{O}_3/\text{Py}$ , the temporal phase of the Py detector voltage  $V(H)$  (i.e., the lock-in phase) in response to the periodic thermal drive of the heater is shown. The phase shows a clear  $\pi$  jump upon magnetization reversal of Py around zero field and remains nearly constant with increasing magnetic field. On top of this flat background, a small resonant [41,42,60,61] feature is conspicuous at the field of  $\sim 30$  kOe. While this anomaly is only observed at high thermal drives indicating a nonlinear phenomenon, it is independently reproduced in the  $\text{Cr}_2\text{O}_3/\text{Py}/\text{Pt}$  control sample [Fig. 5(b)]. Strikingly, the field at which the anomaly is observed corresponds to the crossing of the LH antiferromagnetic magnons of  $\text{Cr}_2\text{O}_3$  and the ferromagnetic magnons of Py in the frequency-field diagram [Fig. 4(c)]. The observed anomaly points to a resonant (partial) hybridization [39] of the antiferromagnetic LH magnons of  $\text{Cr}_2\text{O}_3$  and ferromagnetic magnons of Py, as such hybridization would modify the effective (combined via phonons and magnons) thermal

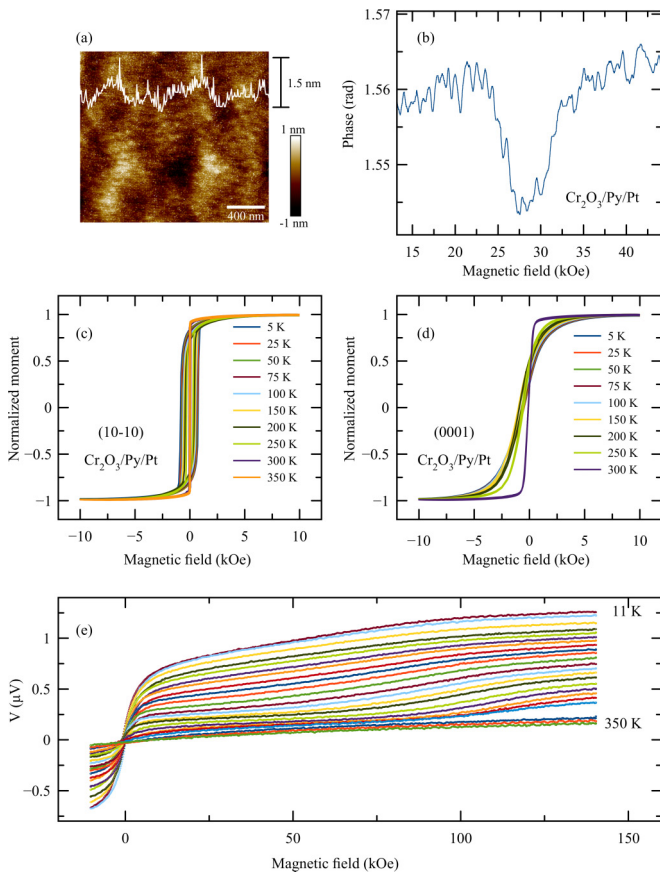


FIG. 5. (a) Atomic force micrograph of the Cr<sub>2</sub>O<sub>3</sub> surface, including a line scan. (b) The phase of the thermal signal from the Cr<sub>2</sub>O<sub>3</sub>/Py/Pt control sample shows a resonant feature near 30 kOe. (c,d) Magnetometry of Cr<sub>2</sub>O<sub>3</sub>/Py/Pt along [10 $\bar{1}$ 0] and [0001] directions. (e) Thermal signal from the Cr<sub>2</sub>O<sub>3</sub>/Py/Pt control sample shows a similar behavior to that of the Cr<sub>2</sub>O<sub>3</sub>/Py sample.

transport and thus lead to a phase shift of the the thermal wave [62] from Py into Cr<sub>2</sub>O<sub>3</sub>. The frequency-field diagram [Fig. 4(c)] shows no crossing of the (zero-wave-vector) QFM magnons of Cr<sub>2</sub>O<sub>3</sub> and the ferromagnetic magnons of Py, suggesting that the magnonic spin current above the SF transition is facilitated in a nonresonant manner. Recently, resonant and nonresonant magnon transduction at an interface of dissimilar ferromagnets has been observed [40,41]; our results suggest that analogous phenomena are possible at AFM/FM interfaces.

## V. CONCLUSIONS

In summary, we have demonstrated thermally driven spin injection from a metallic ferromagnet into an insulating antiferromagnet. The interfacial spin current is converted into voltage signals via spin-orbit effects in Py. The spin injection in the AFM/FM system grows with increasing temperature and allows for sizable signals at room temperature. This is in stark contrast to AFM/NM systems where sizable spin transport has only been shown in the narrow range of cryogenic temperatures. Realization of robust spin transport near room temperature in thin film systems is an important step toward practical AFM-based spintronic devices,

in particular AFM-based spin-torque devices. Our theoretical model as well as experimental observation of coupling between the magnonic subsystems in the Cr<sub>2</sub>O<sub>3</sub>/Py hybrid suggest that interfacial magnon transduction plays an important role in the spin transport. Our results motivate further studies to elucidate the microscopic mechanisms of the spin transport across AFM/FM interfaces, including magnon coupling and transduction. Our work opens avenues for spintronic and quantum information [63–65] applications based on hybrid ferromagnet/antiferromagnet systems and merges spin-orbitronic concepts of ferromagnetic metals with antiferromagnetic spintronics.

## ACKNOWLEDGMENTS

This work was supported by the National Science Foundation through Grant No. ECCS-1810541. H.Z. and R.C. are supported by the Air Force Office of Scientific Research under Grant No. FA9550-19-1-0307. W.Y. and J.S. acknowledge support by DOE BES Award No. DE-FG02-07ER46351. The authors thank Annette Kunz for TEM specimen preparation. Furthermore, the use of the HZDR Ion Beam Center TEM facilities is acknowledged.

## APPENDIX

*Material growth parameters.* The Cr<sub>2</sub>O<sub>3</sub> thin films were deposited on *m*-plane sapphire substrates by rf magnetron sputtering at 700 °C. The base pressure was  $3 \times 10^{-8}$  mbar and the working pressure of Ar gas was  $5 \times 10^{-3}$  mbar; nominal sputter rate was set to 1.72 nm/min. Prior to the deposition, the substrates were annealed at 750 °C for 10 min. Detector layers were magnetron sputtered at room temperature (dc for Py and rf for Pt) at Ar gas working pressure of  $8 \times 10^{-4}$  mbar. For oxidation-prone materials, a 5 nm sputtered Al<sub>2</sub>O<sub>3</sub> cap layer was used.

*Device fabrication.* We fabricated SSE devices from the films using a combination of an optical lithography mask and negative photoresist for the detector layer. Once the  $2.4 \times 0.25$  mm<sup>2</sup> bar had been developed, the detector layer was ion milled down to Cr<sub>2</sub>O<sub>3</sub>, leaving only the detector bar on top of the Cr<sub>2</sub>O<sub>3</sub> layer. Using atomic layer deposition, an 80 nm electrically insulating layer of Al<sub>2</sub>O<sub>3</sub> was deposited. Lastly, the heater layer was deposited in similar fashion to the detector except using positive photoresist and magnetron sputtering for the metallization.

*Material characterization.* The resistivity of the Py detector, sandwiched between Cr<sub>2</sub>O<sub>3</sub> and Al<sub>2</sub>O<sub>3</sub>, was measured with the two-point method (with wire bonds through the Al<sub>2</sub>O<sub>3</sub> layer) and may be contaminated with contact resistance. The thus upper limit of the resistivity was obtained as  $\sim 1 \mu\Omega$  m which is 2–3 times larger than the literature values of pristine Py films [66] and in agreement with resistivity of Py grown under similar conditions on oxide substrates [67–69].

The atomic force microscopy of the Cr<sub>2</sub>O<sub>3</sub> film surface is shown in Fig. 5(a).

Cross-sectional bright-field and high-resolution transmission electron microscopy (TEM) measurements were performed using an image-C<sub>s</sub>-corrected Titan 80-300 microscope (FEI: Field Electron and Ion Company) operated at

an accelerating voltage of 300 kV. Prior to TEM analysis, the specimen was mounted in a double-tilt low-background holder and placed for 8 s into a Model 1020 Plasma Cleaner (Fischione) to remove possible contaminations. The cross-sectional TEM specimen was prepared by *in situ* lift-out using a Helios 5 CX focused ion beam (FIB) device (Thermo Fisher). To protect the sample surface, a carbon cap layer was deposited beginning with electron-beam-assisted and subsequently followed by Ga-FIB-assisted precursor decomposition. Afterwards, the TEM lamella was prepared using a 30 keV Ga FIB with adapted currents. Its transfer to a three-post copper lift-out grid (Omniprobe) was done with an EasyLift EX nanomanipulator (Thermo Fisher). To minimize sidewall damage, Ga ions with only 5 keV energy were used for final thinning of the TEM lamella to electron transparency.

The hysteresis curves of the Cr<sub>2</sub>O<sub>3</sub>/Py/Pt show exchange bias for magnetic fields applied parallel to the *c*-axis [compare Figs. 5(c) and 5(d)].

**Theoretical model.** Equation (5) encompasses two contributions: The ANE (the second term) is a Py volume effect independent of Cr<sub>2</sub>O<sub>3</sub>, which is responsible for the background signal. The SAHE component (the first term), on the other hand, depends on the interfacial spin injection  $j_s^0$  and hence on the Néel vector in Cr<sub>2</sub>O<sub>3</sub>. The SF transition in Cr<sub>2</sub>O<sub>3</sub> directly leads to a sign change of  $j_s^0$ , because the reorientation of the Néel vector causes a reversal of the spin polarization of the lowest-energy magnon bands [25], as shown in Fig. 6(a) calculated at 10 K using the formalism developed in Ref. [27]. This formalism becomes less accurate when approaching the Néel temperature, which is represented by the dashed shading in Fig. 3(e).

**Thermal signal and control samples.** We find the SSE signals of both Cr<sub>2</sub>O<sub>3</sub>/Py and Cr<sub>2</sub>O<sub>3</sub>/Pt to be anti-symmetric with respect to the polarity of the applied magnetic field, as shown in Figs. 6(c) and 6(d). The thermal signal was measured on a control sample with a Py detector layer deposited directly onto an *m*-plane sapphire substrate. The data in Fig. 6(b) show a steplike signal, indicative of Py magnetization reversal near zero field.

The misalignment procedure shown in Fig. 3(a) is time intensive and does not result in a quantitative determination of the SSE signal magnitudes, since the the ANE contribution itself is angle dependent and the misalignment results in partial but not full suppression of the SSE signal. We thus extract the magnitude difference of the thermal signal below and above the spin-flop transition from spectra with magnetic field fully aligned with the *c*-axis of Cr<sub>2</sub>O<sub>3</sub>. This approach

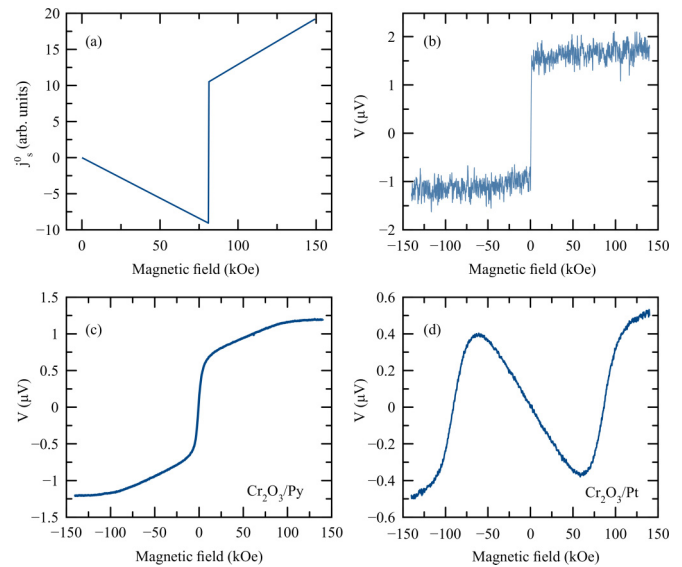


FIG. 6. (a) Calculated interfacial spin current at 10 K. (b) Thermal signal due to anomalous Nernst effect (ANE) from the Al<sub>2</sub>O<sub>3</sub>/Py control sample at 10 K shows steplike reversal of magnetization. (c) SSE signals of the Cr<sub>2</sub>O<sub>3</sub>/Py and (d) Cr<sub>2</sub>O<sub>3</sub>/Pt sample are anti-symmetric with respect to the magnetic field polarity.

returns the qualitative behavior, conspicuous from the raw data in Figs. 2(a) and 5(e). The inaccuracy of this heuristic approach results in error bars due to finite width of the SF transition. The upper error bar is generally larger because the limited field range does not allow for extrapolating the behavior above the SF, especially at higher temperatures. The ANE background is not truly subtracted but, given the antagonical temperature dependences of the SSE and ANE contributions, the procedure allows us to assert that the magnitude for the maximum SSE signal in Cr<sub>2</sub>O<sub>3</sub>/Py near room temperature is comparable to that in Cr<sub>2</sub>O<sub>3</sub>/Pt at low temperature.

For extracting the spin-flop field of the Cr<sub>2</sub>O<sub>3</sub>/Py sample, we smooth the raw data, calculate the derivative, and evaluate the position of the local maximum (i.e., the inflection point of the raw data) corresponding to the spin-flop field. The data are plotted in Fig. 2(c).

The thermal signal was measured on a control sample of Cr<sub>2</sub>O<sub>3</sub>/Py/Pt. The data in Fig. 5(e) show a behavior similar to that observed in the Cr<sub>2</sub>O<sub>3</sub>/Py sample.

The phase of the thermal signal of the Cr<sub>2</sub>O<sub>3</sub>/Py/Pt in Fig. 5(b) shows an anomaly at  $\sim 30$  kOe similar to that of the Cr<sub>2</sub>O<sub>3</sub>/Py sample.

- [1] V. Baltz, A. Manchon, M. Tsoi, T. Moriyama, T. Ono, and Y. Tserkovnyak, Antiferromagnetic spintronics, *Rev. Mod. Phys.* **90**, 015005 (2018).
- [2] L. Fallarino, A. Berger, and C. Binek, Giant temperature dependence of the spin reversal field in magnetoelectric chromia, *Appl. Phys. Lett.* **104**, 022403 (2014).
- [3] A. Brataas, B. van Wees, O. Klein, G. de Loubens, and M. Viret, Spin insulatronics, *Phys. Rep.* **885**, 1 (2020).
- [4] D. Hou, Z. Qiu, and E. Saitoh, Spin transport in antiferromagnetic insulators: progress and challenges, *NPG Asia Mater.* **11**, 35 (2019).
- [5] F. Hellman, A. Hoffmann, Y. Tserkovnyak, G. S. D. Beach, E. E. Fullerton, C. Leighton, A. H. MacDonald, D. C. Ralph, D. A. Arena, H. A. Dürr, P. Fischer, J. Grollier, J. P. Heremans, T. Jungwirth, A. V. Kimel, B. Koopmans, I. N. Krivorotov, S. J. May, A. K. Petford-Long, J. M. Rondinelli *et al.*, Interface-induced phenomena in magnetism, *Rev. Mod. Phys.* **89**, 025006 (2017).
- [6] A. Navabi, Y. Liu, P. Upadhyaya, K. Murata, F. Ebrahimi, G. Yu, B. Ma, Y. Rao, M. Yazdani, M. Montazeri, L. Pan, I. N. Krivorotov, I. Barsukov, Q. Yang, P. Khalili Amiri, Y. Tserkovnyak, and K. L. Wang, Control of Spin-Wave Damping

- in YIG Using Spin Currents from Topological Insulators, *Phys. Rev. Applied* **11**, 034046 (2019).
- [7] A. M. Gonçalves, F. Garcia, H. K. Lee, A. Smith, P. R. Soledade, C. A. C. Passos, M. Costa, N. M. Souza-Neto, I. N. Krivorotov, L. C. Sampaio, and I. Barsukov, Oscillatory inter-layer coupling in spin Hall systems, *Sci. Rep.* **8**, 2318 (2018).
- [8] J. Fischer, O. Gomonay, R. Schlitz, K. Ganzhorn, N. Vlietstra, M. Althammer, H. Huebl, M. Opel, R. Gross, S. T. B. Goennenwein, and S. Geprägs, Spin Hall magnetoresistance in antiferromagnet/heavy-metal heterostructures, *Phys. Rev. B* **97**, 014417 (2018).
- [9] L. Baldrati, A. Ross, T. Niizeki, C. Schneider, R. Ramos, J. Cramer, O. Gomonay, M. Filianina, T. Savchenko, D. Heinze, A. Kleibert, E. Saitoh, J. Sinova, and M. Kläui, Full angular dependence of the spin hall and ordinary magnetoresistance in epitaxial antiferromagnetic NiO(001)/Pt thin films, *Phys. Rev. B* **98**, 024422 (2018).
- [10] L. Baldrati, O. Gomonay, A. Ross, M. Filianina, R. Lebrun, R. Ramos, C. Leveille, F. Fuhrmann, T. R. Forrest, F. Maccherozzi, S. Valencia, F. Kronast, E. Saitoh, J. Sinova, and M. Kläui, Mechanism of Néel Order Switching in Antiferromagnetic Thin Films Revealed by Magnetotransport and Direct Imaging, *Phys. Rev. Lett.* **123**, 177201 (2019).
- [11] P. Zhang, J. Finley, T. Safi, and L. Liu, Quantitative Study on Current-Induced Effect in an Antiferromagnet Insulator/Pt Bilayer Film, *Phys. Rev. Lett.* **123**, 247206 (2019).
- [12] H. Meer, F. Schreiber, C. Schmitt, R. Ramos, E. Saitoh, O. Gomonay, J. Sinova, L. Baldrati, and M. Kläui, Direct imaging of current-induced antiferromagnetic switching revealing a pure thermomagnetoelastic switching mechanism in NiO, *Nano Lett.* **21**, 114 (2021).
- [13] E. Cogulu, N. N. Statuto, Y. Cheng, F. Yang, R. V. Chopdekar, H. Ohldag, and A. D. Kent, Direct imaging of electrical switching of antiferromagnetic Néel order in  $\alpha$ -Fe<sub>2</sub>O<sub>3</sub> epitaxial films, *Phys. Rev. B* **103**, L100405 (2021).
- [14] C. Schmitt, L. Baldrati, L. Sanchez-Tejerina, F. Schreiber, A. Ross, M. Filianina, S. Ding, F. Fuhrmann, R. Ramos, F. Maccherozzi, D. Backes, M.-A. Mawass, F. Kronast, S. Valencia, E. Saitoh, G. Finocchio, and M. Kläui, Identification of Néel Vector Orientation in Antiferromagnetic Domains Switched by Currents in NiO/Pt Thin Films, *Phys. Rev. Applied* **15**, 034047 (2021).
- [15] B. J. Jacot, G. Krishnaswamy, G. Sala, C. O. Avci, S. Vélez, P. Gambardella, and C.-H. Lambert, Systematic study of non-magnetic resistance changes due to electrical pulsing in single metal layers and metal/antiferromagnet bilayers, *J. Appl. Phys.* **128**, 173902 (2020).
- [16] C. C. Chiang, S. Y. Huang, D. Qu, P. H. Wu, and C. L. Chien, Absence of Evidence of Electrical Switching of the Antiferromagnetic Néel Vector, *Phys. Rev. Lett.* **123**, 227203 (2019).
- [17] R. Khymyn, I. Lisenkov, V. S. Tiberkevich, A. N. Slavin, and B. A. Ivanov, Transformation of spin current by antiferromagnetic insulators, *Phys. Rev. B* **93**, 224421 (2016).
- [18] K. S. Das, F. Feringa, M. Middelkamp, B. J. van Wees, and I. J. Vera-Marun, Modulation of magnon spin transport in a magnetic gate transistor, *Phys. Rev. B* **101**, 054436 (2020).
- [19] D. Hou, Z. Qiu, J. Barker, K. Sato, K. Yamamoto, S. Vélez, J. M. Gomez-Perez, L. E. Hueso, F. Casanova, and E. Saitoh, Tunable Sign Change of Spin Hall Magnetoresistance in Pt/NiO/YIG Structures, *Phys. Rev. Lett.* **118**, 147202 (2017).
- [20] H. Reichlova, R. Schlitz, and S. T. B. Goennenwein, Spin current in an antiferromagnet is coherent, *Physics* **13**, 83 (2020).
- [21] S. T. B. Goennenwein and G. E. W. Bauer, Electron spins blow hot and cold, *Nat. Nanotechnol.* **7**, 145 (2012).
- [22] S. M. Wu, W. Zhang, A. KC, P. Borisov, J. E. Pearson, J. S. Jiang, D. Lederman, A. Hoffmann, and A. Bhattacharya, Antiferromagnetic Spin Seebeck Effect, *Phys. Rev. Lett.* **116**, 097204 (2016).
- [23] C. Liu, Y. Luo, D. Hong, S. Zhang, B. Fisher, A. Hoffmann, A. Bhattacharya *et al.*, Electric-field control of magnon spin current in an antiferromagnetic insulator, *Sci. Adv.* **7**, eabg1669 (2021).
- [24] P. Muduli, R. Schlitz, T. Kosub, R. Hübner, A. Erbe, D. Makarov, and S. T. B. Goennenwein, Local and nonlocal spin seebeck effect in lateral Pt-Cr<sub>2</sub>O<sub>3</sub>-Pt devices at low temperatures, *APL Mater.* **9**, 021122 (2021).
- [25] J. Li, C. Blake Wilson, R. Cheng, M. Lohmann, M. Kavand, W. Yuan, M. Aldosary, N. Agladze, P. Wei, M. S. Sherwin, and J. Shi, Spin current from sub-terahertz-generated antiferromagnetic magnons, *Nature (London)* **578**, 70 (2020).
- [26] W. Yuan, J. Li, and J. Shi, Spin current generation and detection in uniaxial antiferromagnetic insulators, *Appl. Phys. Lett.* **117**, 100501 (2020).
- [27] D. Reitz, J. Li, W. Yuan, J. Shi, and Y. Tserkovnyak, Spin seebeck effect near the antiferromagnetic spin-flop transition, *Phys. Rev. B* **102**, 020408(R) (2020).
- [28] I. Boventer, H. T. Simensen, A. Anane, M. Kläui, A. Brataas, and R. Lebrun, Room-Temperature Antiferromagnetic Resonance and Inverse Spin-Hall Voltage in Canted Antiferromagnets, *Phys. Rev. Lett.* **126**, 187201 (2021).
- [29] T. Taniguchi, J. Grollier, and M. D. Stiles, Spin-Transfer Torques Generated by the Anomalous Hall Effect and Anisotropic Magnetoresistance, *Phys. Rev. Applied* **3**, 044001 (2015).
- [30] A. Manchon, J. Železný, I. M. Miron, T. Jungwirth, J. Sinova, A. Thiaville, K. Garello, and P. Gambardella, Current-induced spin-orbit torques in ferromagnetic and antiferromagnetic systems, *Rev. Mod. Phys.* **91**, 035004 (2019).
- [31] T. Taniguchi, Magnetoresistance originated from charge-spin conversion in ferromagnet, *AIP Adv.* **8**, 055916 (2018).
- [32] X. R. Wang, Anomalous spin Hall and inverse spin Hall effects in magnetic systems, *Commun. Phys.* **4**, 55 (2021).
- [33] J. D. Gibbons, D. MacNeill, R. A. Buhrman, and D. C. Ralph, Reorientable Spin Direction for Spin Current Produced by the Anomalous Hall Effect, *Phys. Rev. Applied* **9**, 064033 (2018).
- [34] A. Bose, D. D. Lam, S. Bhuktare, S. Dutta, H. Singh, Y. Jibiki, M. Goto, S. Miwa, and A. A. Tulapurkar, Observation of Anomalous Spin Torque Generated by a Ferromagnet, *Phys. Rev. Applied* **9**, 064026 (2018).
- [35] C. Safranski, E. A. Montoya, and I. N. Krivorotov, Spin-orbit torque driven by a planar Hall current, *Nat. Nanotechnol.* **14**, 27 (2019).
- [36] K. S. Das, W. Y. Schoemaker, B. J. van Wees, and I. J. Vera-Marun, Spin injection and detection via the anomalous spin Hall effect of a ferromagnetic metal, *Phys. Rev. B* **96**, 220408(R) (2017).
- [37] C. Safranski, I. Barsukov, H. K. Lee, T. Schneider, A. A. Jara, A. Smith, H. Chang, K. Lenz, J. Lindner, Y. Tserkovnyak, M. Wu, and I. N. Krivorotov, Spin caloritronic nano-oscillator, *Nat. Commun.* **8**, 117 (2017).

- [38] B. Arkook, C. Safranski, R. Rodriguez, I. N. Krivorotov, T. Schneider, K. Lenz, J. Lindner, H. Chang, M. Wu, Y. Tserkovnyak, and I. Barsukov, Thermally driven two-magnet nano-oscillator with large spin-charge conversion, [arXiv:1909.12445](https://arxiv.org/abs/1909.12445).
- [39] Y. Li, W. Cao, V. P. Amin, Z. Zhang, J. Gibbons, J. Sklenar, J. Pearson, P. M. Haney, M. D. Stiles, W. E. Bailey, V. Novosad, A. Hoffmann, and W. Zhang, Coherent Spin Pumping in a Strongly Coupled Magnon-Magnon Hybrid System, *Phys. Rev. Lett.* **124**, 117202 (2020).
- [40] L. Liu, T. Moriyama, D. C. Ralph, and R. A. Buhrman, Spin-Torque Ferromagnetic Resonance Induced by the Spin Hall Effect, *Phys. Rev. Lett.* **106**, 036601 (2011).
- [41] Y. Fan, J. Finley, J. Han, M. E. Holtz, P. Quarterman, P. Zhang, T. S. Safi, J. T. Hou, A. J. Grutter, and L. Liu, Resonant spin transmission mediated by magnons in a magnetic insulator multilayer structure, *Adv. Mater.* **33**, 2008555 (2021).
- [42] A. Etesamirad, R. Rodriguez, J. Bocanegra, R. Verba, J. Katine, I. N. Krivorotov, V. Tyberkevych, B. Ivanov, and I. Barsukov, Controlling magnon interaction by a nanoscale switch, *ACS Appl. Mater. Interfaces* **13**, 20288 (2021).
- [43] J. Cramer, F. Fuhrmann, U. Ritzmann, V. Gall, T. Niizeki, R. Ramos, Z. Qiu, D. Hou, T. Kikkawa, J. Sinova, U. Nowak, E. Saitoh, and M. Kläui, Magnon detection using a ferroic collinear multilayer spin valve, *Nat. Commun.* **9**, 1089 (2018).
- [44] G. E. W. Bauer, E. Saitoh, and B. J. van Wees, Spin caloritronics, *Nat. Mater.* **11**, 391 (2012).
- [45] K. Uchida, S. Takahashi, K. Harii, J. Ieda, W. Koshibae, K. Ando, S. Maekawa, and E. Saitoh, Observation of the spin Seebeck effect, *Nature (London)* **455**, 778 (2008).
- [46] S. M. Rezende, R. L. Rodríguez-Suárez, and A. Azevedo, Theory of the spin Seebeck effect in antiferromagnets, *Phys. Rev. B* **93**, 014425 (2016).
- [47] J. Holanda, O. Alves Santos, R. O. Cunha, J. B. S. Mendes, R. L. Rodríguez-Suárez, A. Azevedo, and S. M. Rezende, Longitudinal spin Seebeck effect in permalloy separated from the anomalous Nernst effect: Theory and experiment, *Phys. Rev. B* **95**, 214421 (2017).
- [48] S. L. Yin, Q. Mao, Q. Y. Meng, D. Li, and H. W. Zhao, Hybrid anomalous and planar nernst effect in permalloy thin films, *Phys. Rev. B* **88**, 064410 (2013).
- [49] I. Barsukov, Y. Fu, A. M. Gonçalves, M. Spasova, M. Farle, L. C. Sampaio, R. E. Arias, and I. N. Krivorotov, Field-dependent perpendicular magnetic anisotropy in CoFeB thin films, *Appl. Phys. Lett.* **105**, 152403 (2014).
- [50] J. M. Shaw, H. T. Nembach, T. J. Silva, and C. T. Boone, Precise determination of the spectroscopic  $g$ -factor by use of broadband ferromagnetic resonance spectroscopy, *J. Appl. Phys.* **114**, 243906 (2013).
- [51] I. Barsukov, Y. Fu, C. Safranski, Y.-J. Chen, B. Youngblood, A. M. Gonçalves, M. Spasova, M. Farle, J. A. Katine, C. C. Kuo, and I. N. Krivorotov, Magnetic phase transitions in Ta/CoFeB/MgO multilayers, *Appl. Phys. Lett.* **106**, 192407 (2015).
- [52] J. Nogués and I. K. Schuller, Exchange bias, *J. Magn. Magn. Mater.* **192**, 203 (1999).
- [53] W. Yuan, T. Su, Q. Song, W. Xing, Y. Chen, T. Wang, Z. Zhang, X. Ma, P. Gao, J. Shi, and W. Han, Crystal structure manipulation of the exchange bias in an antiferromagnetic film, *Sci. Rep.* **6**, 28397 (2016).
- [54] S. Foner, High-Field Antiferromagnetic Resonance in  $\text{Cr}_2\text{O}_3$ , *Phys. Rev.* **130**, 183 (1963).
- [55] R. Schlitz, T. Kosub, A. Thomas, S. Fabretti, K. Nielsch, D. Makarov, and S. T. B. Goennenwein, Evolution of the spin Hall magnetoresistance in  $\text{Cr}_2\text{O}_3/\text{Pt}$  bilayers close to the Néel temperature, *Appl. Phys. Lett.* **112**, 132401 (2018).
- [56] A. N. Bogdanov, A. V. Zhuravlev, and U. K. Röbber, Spin-flop transition in uniaxial antiferromagnets: Magnetic phases, reorientation effects, and multidomain states, *Phys. Rev. B* **75**, 094425 (2007).
- [57] Y. Cheng, R. Zarzuela, J. T. Brangham, A. J. Lee, S. White, P. C. Hammel, Y. Tserkovnyak, and F. Yang, Nonsinusoidal angular dependence of FMR-driven spin current across an antiferromagnet in  $\text{Y}_3\text{Fe}_5\text{O}_{12}/\text{NiO}/\text{Pt}$  trilayers, *Phys. Rev. B* **99**, 060405(R) (2019).
- [58] R. Cheng, J. Xiao, Q. Niu, and A. Brataas, Spin Pumping and Spin-Transfer Torques in Antiferromagnets, *Phys. Rev. Lett.* **113**, 057601 (2014).
- [59] P. Vaidya, S. A. Morley, J. van Tol, Y. Liu, R. Cheng, A. Brataas, D. Lederman, and E. del Barco, Subterahertz spin pumping from an insulating antiferromagnet, *Science* **368**, 160 (2020).
- [60] I. Barsukov, H. K. Lee, A. A. Jara, Y.-J. Chen, A. M. Gonçalves, C. Sha, J. A. Katine, R. E. Arias, B. A. Ivanov, and I. N. Krivorotov, Giant nonlinear damping in nanoscale ferromagnets, *Sci. Adv.* **5**, eaav6943 (2019).
- [61] J. Chen, C. Liu, T. Liu, Y. Xiao, K. Xia, G. E. W. Bauer, M. Wu, and H. Yu, Strong Interlayer Magnon-Magnon Coupling in Magnetic Metal-Insulator Hybrid Nanostructures, *Phys. Rev. Lett.* **120**, 217202 (2018).
- [62] A. Rosencwaig, Theoretical aspects of photoacoustic spectroscopy, *J. Appl. Phys.* **49**, 2905 (1978).
- [63] Quantum possibilities, *Nat. Phys.* **14**, 321 (2018).
- [64] Z.-L. Xiang, S. Ashhab, J. Q. You, and F. Nori, Hybrid quantum circuits: Superconducting circuits interacting with other quantum systems, *Rev. Mod. Phys.* **85**, 623 (2013).
- [65] G. Kurizki, P. Bertet, Y. Kubo, K. Mølmer, D. Petrosyan, P. Rabl, and J. Schmiedmayer, Quantum technologies with hybrid systems, *Proc. Natl. Acad. Sci. USA* **112**, 3866 (2015).
- [66] G. Nahrwold, J. M. Scholtyssek, S. Motl-Ziegler, O. Albrecht, U. Merkt, and G. Meier, Structural, magnetic, and transport properties of permalloy for spintronic experiments, *J. Appl. Phys.* **108**, 013907 (2010).
- [67] M. Zhang and C. Deng, Magnetic, optical and electrical properties of permalloy films by DC magnetron sputtering, *J. Mater. Sci.: Mater. Electron.* **32**, 4949 (2021).
- [68] A. Guitoum, A. Bourzami, A. Layadi, and G. Schmerber, Structural, electrical and magnetic properties of evaporated permalloy thin films: effect of substrate and thickness, *Eur. Phys. J. Appl. Phys.* **58**, 20301 (2012).
- [69] M. Urse, A. Moga, M. Grigoras, and H. Chiriac, Magnetic and electrical properties of  $[\text{NiFe}/\text{SiO}_2] \times N$  multilayer thin films, *J. Optoelectron. Adv. Mater.* **7**, 759 (2005).